Check for updates

View Article Online
View Journal

Journal of
Materials Chemistry A
Materials for energy and sustainability

Accepted Manuscript

This article can be cited before page numbers have been issued, to do this please use: K. P. Miskin, G. Lemson, T. Arbaugh, E. Ragasa, N. Le and P. Clancy, *J. Mater. Chem. A*, 2026, DOI: 10.1039/D6TA01465H.

Volume 6
Number 12
28 March 2018
Pages 4883-5230

Journal of
Materials Chemistry A
Materials for energy and sustainability
rsc.li/materials-a

ISSN 2050-7488

ROYAL SOCIETY
OF CHEMISTRY

COMMUNICATION
Zhenhai Wen *et al.*
An electrochemically neutralized energy-assisted low-cost acid-alkaline electrolyzer for energy-saving electrolysis hydrogen generation

This is an Accepted Manuscript, which has been through the Royal Society of Chemistry peer review process and has been accepted for publication.

Accepted Manuscripts are published online shortly after acceptance, before technical editing, formatting and proof reading. Using this free service, authors can make their results available to the community, in citable form, before we publish the edited article. We will replace this Accepted Manuscript with the edited and formatted Advance Article as soon as it is available.

You can find more information about Accepted Manuscripts in the Information for Authors.

Please note that technical editing may introduce minor changes to the text and/or graphics, which may alter content. The journal's standard Terms & Conditions and the Ethical guidelines still apply. In no event shall the Royal Society of Chemistry be held responsible for any errors or omissions in this Accepted Manuscript or any consequences arising from the use of any information it contains.

ROYAL SOCIETY
OF CHEMISTRY

rsc.li/materials-a

View Article Online
DOI: 10.1039/D6TA01465H

How Soft Metal Halide Perovskite Lattices Heal Following Energetic Particle Bombardment

Kumar Miskin,[1] Gerard Lemson,[2, 3] Tom Arbaugh,[4] Eugene Ragasa,[4] Nam Q. Le,[4] and Paulette Clancy[5, 1]
[1]*Dept. of Materials Science and Engineering, Johns Hopkins University*
[2]*Institute for Data-Intensive Engineering and Science, Johns Hopkins University*
[3]*Data Science and AI Institute, Johns Hopkins University*
[4]*Johns Hopkins Applied Physics Laboratory*
[5]*Dept. of Chemical and Biomolecular Engineering, Johns Hopkins University*

(Dated: 12 May 2026)

Recent NASA tests have demonstrated the exceptional durability of metal halide perovskite solar cells against space radiation; however, the atomic-level mechanisms governing this resilience remain speculative. Here, we elucidate the self-healing capacity of $CsPbI_3$ under energetic particle bombardment (1 eV to 1000 eV) using large-scale Molecular Dynamics (MD) simulations and a ReaxFF reactive force field. To analyze the resulting massive trajectory datasets, we employ a novel relational database (SQL) framework that enables scalable, query-based interrogation of defect dynamics. Our analysis reveals that the material's radiation hardness arises from the intrinsic softness of the perovskite lattice, specifically the ability of PbI_6 octahedra to dissipate energy through collective tilting and spinning. We observe a strong species-dependent recovery mechanism where ≈32% of displaced halides return to lattice sites within 10 ps, effectively preventing permanent amorphization. Furthermore, we demonstrate that radiation-induced structural disorder correlates quantitatively with classical Glazer tilt systems and matches octahedral distortions observed in experimental nanocrystals. These results explain the material's proven spaceflight performance and establish a powerful computational workflow for analyzing defect tolerance in soft semiconductors

Open Access Article. Published on 15 June 2026. Downloaded on 6/17/2026 5:59:14 AM.
This article is licensed under a Creative Commons Attribution-NonCommercial 3.0 Unported Licence.

Journal of Materials Chemistry A Accepted Manuscript

I. INTRODUCTION

Metal halide perovskites (MHPs) are a class of crystalline semiconductors with the general formula ABX_3, where A is a monovalent cation *(e.g.,* methylammonium, formamidinium, or cesium), B is a divalent metal cation (commonly lead or tin), and X is a halide anion (chloride, bromide, or iodide). The structural stability of a given ABX_3 composition is often described by two geometric descriptors: the Goldschmidt tolerance factor $t = (r_A + r_X)/\sqrt{2}(r_B + r_X)$, which should fall in the range $0.8 \leq t \leq 1.0$ for a stable perovskite phase, and the octahedral factor $\mu = r_B/r_X$, which must exceed ∼0.41 to ensure a stable BX_6 octahedral framework. Together, these two parameters help describe the compositional space within which functional halide perovskites can be realized and provide a quantitative basis to help compare structural rigidity across compositions.[1]

These materials have garnered substantial interest for their exceptional optoelectronic properties, including high absorption coefficients, tunable band gaps, long carrier diffusion lengths, and low trap densities.[2–5] Combined with their solution processability, low-cost precursors, and scalable fabrication routes, MHPs have rapidly achieved power conversion efficiencies exceeding 25% in photovoltaic devices.[6] Beyond terrestrial applications, MHPs have emerged as compelling candidates for space power systems owing to their lightweight nature, mechanical flexibility, and suitability for tandem configurations.[7] Critically, unlike conventional Si-based or III-V semiconductors, MHPs are intrinsically "soft" materials that exhibit defect self-healing mechanisms enabling at least partial recovery from radiation-induced damage—a property of clear value in the harsh radiation environment of space.[8,9]

Experimental evidence for this radiation resilience has grown steadily. Stratospheric mission testing by Cardinaletti *et al.*[10] established early performance benchmarks, and the landmark 10-month spaceflight test by Delmas *et al.*[8] confirmed that MHP solar cells can sustain performance under prolonged particle bombardment in extra-terrestrial conditions. More recently, deposition of a micron-thick silicon oxide overlayer has been shown to further harden MHPs—including $Cs_{0.05}(MA_{0.17}FA_{0.83})_{0.95}Pb(I_{0.83}Br_{0.17})_3$ and $CsPbI_2Br$—against α-radiation, water, and atomic oxygen without sacrificing power conversion efficiency.[11] Despite these advances, computational investigations probing the fundamental atomic-scale mechanisms behind this resilience remain sparse.[12] The properties of MHPs that make them radiation-tolerant are intimately tied to their defect physics: conductivity in MHPs occurs via both electronic and ionic species, and the relatively low formation energies of halide vacancies and interstitials generate mobile charged and neutral species that migrate within and beyond the perovskite layer.[13,14] It remains a major challenge to connect these atomic-scale defect dynamics to macroscopic device behavior, yet it is precisely these processes that govern changes in material composition, structure, and performance over time.

A comprehensive understanding of radiation-matter interactions in MHPs requires examining primary damage—the defects produced immediately after an initial atomic displacement event triggered by a high-energy particle.[15] Molecular dynamics (MD) simulations offer a powerful tool for investigating these complex atomic-level processes, providing depth-dependent defect profiles and insight into how chemical composition and incident particle energy govern radiation tolerance.[12,15–17] However, large-scale MD of radiation events in systems of hundreds of thousands of atoms generates trajectory datasets on the order of 50 GB per simulation, mak-

View Article Online
DOI: 10.1039/D6TA01465H

Open Access Article. Published on 15 June 2026. Downloaded on 6/17/2026 5:59:14 AM.
This article is licensed under a Creative Commons Attribution-NonCommercial 3.0 Unported Licence.

Journal of Materials Chemistry A Accepted Manuscript

ing conventional in-memory analysis workflows impractical. Efficiently interrogating such data demands a scalable, query-based framework—a capability that has not previously been applied in this context.

In this work, we focus on $CsPbI_3$ as our model system—an all-inorganic MHP that is an attractive candidate for space photovoltaics due to its high-temperature stability.[16,18,19] From a computational standpoint, modeling $CsPbI_3$ is uniquely tractable: A validated reactive force field (ReaxFF) exists for this perovskite member,[20] capturing bond -formation, -breaking, and charge transfer processes essential for modeling irradiation conditions. Alternative approaches are either insufficiently accurate—a semi-empirical model such as AMOEBA,[21] for instance, fails to reproduce the *ab initio* preference for stabilizing lower-order lead species[22]—or far too resource-intensive for the length and time scales required here, as would be the case for *ab initio* MD. ReaxFF models for MHPs are currently limited to $CsPbI_3$ and mixed halide CsPbBr-I,[23] making $CsPbI_3$ the natural and well-justified choice for this study.

The central question driving this work is: Which atomic-level mechanisms enable perovskites to maintain structural integrity under high-energy particle bombardment? To answer this, we conduct large-scale MD simulations spanning impact energies from 1 eV to 1 keV and introduce a novel Structured Query Language (SQL)-based data framework that enables scalable, query-driven analysis of the full multi-hundred-GB trajectory dataset. As we shall show below, our results reveal that the intrinsic "softness" of the perovskite lattice—specifically, the collective tilting and spinning of PbI_6 octahedra—are the primary energy dissipation pathways that underlie radiation hardness. We shall demonstrate that $\approx$32% of displaced halide atoms recover to halide lattice sites within 10 ps, effectively suppressing permanent amorphization, and that radiation-induced structural disorder maps quantitatively onto classical Glazer tilt systems. The latter finding is consistent with experimental observations for nanocrystals.[24] These findings provide a mechanistic explanation relevant to space-flight performance of MHP solar cells and establish a transferable computational workflow for assessing defect tolerance in soft semiconductors.

II. METHODOLOGY

This work addresses the lack of mechanistic knowledge regarding the effects of energetic particle impacts on MHP lattices in a vacuum and their subsequent damage recovery. For this study, we used two different but complementary computational techniques: (i) Large-scale molecular dynamics (MD) simulations using a REAX-FF intermolecular potential model to identify primary defect structures induced by energetic particle impacts. (ii) Elucidating the atomistic mechanisms responsible for the defect tolerance we observed, explored using the relational database, Structured Query Language (SQL).[25] As a result, our study provides a quantitative framework for evaluating radiation hardness in metal halide perovskites, which is critical for their deployment in space environments.

A. Molecular Dynamics Simulations

Molecular Dynamics (MD) simulations were designed to capture atomic-scale dynamics of a system under non-equilibrium conditions.[26] Here, our goal is to start by modeling radiation damage in $CsPbI_3$ caused by the impact of energetic particles and the subsequent identification of any partial or complete "defect healing" that occurs after the impact and within a timescale accessible to MD.

The MD simulations that form the heart of this study were conducted using the well-known Sandia MD software package called Large-scale Atomic/Molecular Massively Parallel Simulator (LAMMPS).[27] As mentioned above, the $CsPbI_3$ system can be modeled using a ReaxFF potential.[28] ReaxFF parameterization captures bond formation, bond dissociation, and charge transfer processes critical for describing halide perovskites under irradiation conditions. We have used this model recently to study defects in $CsPbI_3$ with some success, including validation of experimental data.[14]

The simulation cell contained approximately 500,000 atoms, a large system needed to contain the spread of damage to the system following the impact with an energetic particle. The cubic system had dimensions of 301.21 Å, in each of the x, y, z directions. We deployed periodic boundary conditions along the $x-$ and $y-$ axes and non-periodic along $z-$ to expose two free surfaces. No explicit vacuum slab was introduced; the non-periodic $z-$ boundaries create free surfaces where the impact occurs.

After generating an initial, perfect crystalline structure representative of a $CsPbI_3$ perovskite lattice, the system was thermally equilibrated using an isobaric-isothermal NPT ensemble at 500 K and 1 bar for 100,000 time steps of 1 fs each. This was followed by an isothermal NVT ensemble for an additional 10,000 time steps at 300 K to ensure thermal stability. Primary knock-on atom (PKA) events[29] were initiated with recoil energies ranging from 1 eV to 1 keV, representative of particle irradiation in the low-earth orbit (LEO) space environment.[30] While the classical ReaxFF molecular dynamics framework accurately captures nuclear collision cascades and defect generation processes, it does not explicitly account for electronic effects such as electron scattering, ionization, or electronic stopping. These effects become increasingly important at significantly higher irradiation energies, whereas the low-energy regime studied here remains predominantly governed by nuclear stopping interactions. Therefore, the PKA framework provides a physically relevant approximation for evaluating radiation-induced structural damage in $CsPbI_3$ under LEO conditions. A more detailed discussion of these limitations and their implications is provided in the Supplemental Information.

It is worth clarifying the relationship between our PKA approach and an explicit ion bombardment simulation. In the PKA recoil cascade methodology employed here, kinetic energy equivalent to that deposited by an incident particle is imparted to atoms within a hemispherical impact region. The

View Article Online
DOI: 10.1039/D6TA01465H

Open Access Article. Published on 15 June 2026. Downloaded on 6/17/2026 5:59:14 AM.
This article is licensed under a Creative Commons Attribution-NonCommercial 3.0 Unported Licence.

Journal of Materials Chemistry A Accepted Manuscript

resulting displacement cascade is propagated through the lattice under the ReaxFF potential. This is the standard approach used in the radiation damage MD literature.[15] This approach is physically appropriate because, for the energy range studied here (1 eV to 1 keV), "nuclear stopping" dominates. That is, the incident particle transfers its energy to target nuclei through elastic collisions rather than through electronic excitation. It is this recoil energy that drives defect formation. The PKA approach directly captures this nuclear stopping cascade without requiring the incident particle to be explicitly propagated through the cell. Alternate approaches are problematic, as discussed in the Supplemental Information.

To simulate the impact of an energetic particle as will occur in space, a hemispherical region at the top surface was selected as the impact region. Its center was aligned at the midpoint of the $x-$ and y-axes and at the highest z-coordinate (*i.e.,* the top of the box). Kinetic energy was imparted to atoms within a radius of 5 Å of the impact region in order to simulate the particle's impact. Then the system was allowed to evolve in the MD simulation for 10,000 additional time steps. Eight different impact energies were considered: 1, 10, 25, 50, 75, 100, 500, and 1000 eV. In each case, we examined the system for defect generation at each of the impact energy values we investigated.

Post-simulation analyses included atomic displacement tracking during equilibration and impact, radial distribution function (RDF) analysis to evaluate bond length distributions, and Steinhardt order parameter calculations to quantify structural disorder.[15] Defect populations and species-specific energy absorption were also quantified in order to determine dominant energy dissipation pathways. Needless to say, a system of approximately 500,000 atoms followed for 10,000 timesteps, with per-atom positions, velocities, charges, and energies recorded, generates an exceptionally large dataset. Each simulation produced on the order of 50 GB of trajectory data in its original ASCII LAMMPS dump format, corresponding to several hundred GB across the full set of impact energies studied. After conversion to compressed columnar Parquet format, individual simulations were reduced to approximately 16 GB, yet the aggregate dataset remained in the multi-hundred-GB range.

This data volume renders conventional in-memory parsing workflows inefficient and motivates the incorporation of a Structured Query Language (SQL)–based framework,[31] described in the next section, to efficiently interrogate the dynamics and outcomes of the impact and the subsequent re-equilibration.

Trajectories were recorded as LAMMPS dump files at intervals of 0.1–1.0 *ps*, storing atomic positions, velocities, charges, and per-atom energies. This level of resolution was selected to ensure fidelity in tracking fast atomic displacements and subsequent defect recovery events.

B. Data post-processing pipeline

Most of the simulation analysis was carried out on the SciServer platform[32] at the Institute for Data-Intensive Engineering and Science (IDIES) at Johns Hopkins University. SciServer[33] is a collaborative data science platform that provides storage and computational environments tailored to large and custom data sets, enabling server-side analysis and sharing among collaborators. Data sets can also be published through the platform by making them accessible to all SciServer users. SciServer is open-source[34] and is deployed at multiple institutions beyond IDIES. The IDIES instance hosts major data collections, including the Sloan Digital Sky Survey (SDSS), the Johns Hopkins Turbulence Database (JHTDB), the Poseidon ocean circulation simulations, and the Additive Materials Benchmark project.

For this project, dedicated storage was allocated to the collaborators, and the simulation outputs were uploaded in their original format. Data processing and analysis were performed using collaboratively developed Jupyter Python notebooks,[35,36] executed on the platform (dark blue nodes in the workflow shown in Fig. 1).

To enable efficient analysis, the original LAMMPS dump files were converted from the custom ASCII format to the industry-standard Apache Parquet format.[37] Owing to its column-oriented layout and compression, Parquet reduces file sizes from approximately 50 GB to 16 GB. On a typical SciServer compute container, reading a full simulation required about 20 minutes in the original format but only about 1.5 minutes using Parquet.[38]

Although Parquet files can be accessed using the *pandas* library,[39] our analysis primarily relies on DuckDB,[40] which supports direct SQL queries on Parquet data. SQL enables declarative specification of data subsets, allowing DuckDB to optimize query execution and reduce I/O by avoiding full file scans. Joins and aggregate calculations are performed directly within queries, minimizing the need to load large intermediate data sets into memory.

DuckDB also supports user-defined Python functions and operates without a dedicated database server, making it a lightweight and flexible alternative to traditional relational database systems supported by SciServer. While SQL is a standard tool in astronomy—driven by resources such as SDSS—it is less commonly used in materials science; therefore, all key SQL queries used in this work are provided in the Supplemental Information.

DuckDB additionally provides a native storage format that can be generated from Parquet. Its primary advantage is its support for indexing, which can substantially accelerate query execution. We use this format for tasks that benefit from indexing, particularly the identification of octahedra that form the fundamental structural units analyzed in this study.

C. Database definition

The Parquet tables contain columns for the atomic identifier (`id`), time step (`time`), positions (`xs`, `ys`, `zs`), velocities (`vx`, `vy`, `vz`), and atom type (`type`), where types 1, 2, and 3 correspond to A, B, and X atoms, respectively. In addition to these primary tables, supplementary tables were derived to capture statistics of individual atomic orbits. For each atom,

View Article Online
DOI: 10.1039/D6TA01465H

Open Access Article. Published on 15 June 2026. Downloaded on 6/17/2026 5:59:14 AM.
This article is licensed under a Creative Commons Attribution-NonCommercial 3.0 Unported Licence.

Journal of Materials Chemistry A Accepted Manuscript

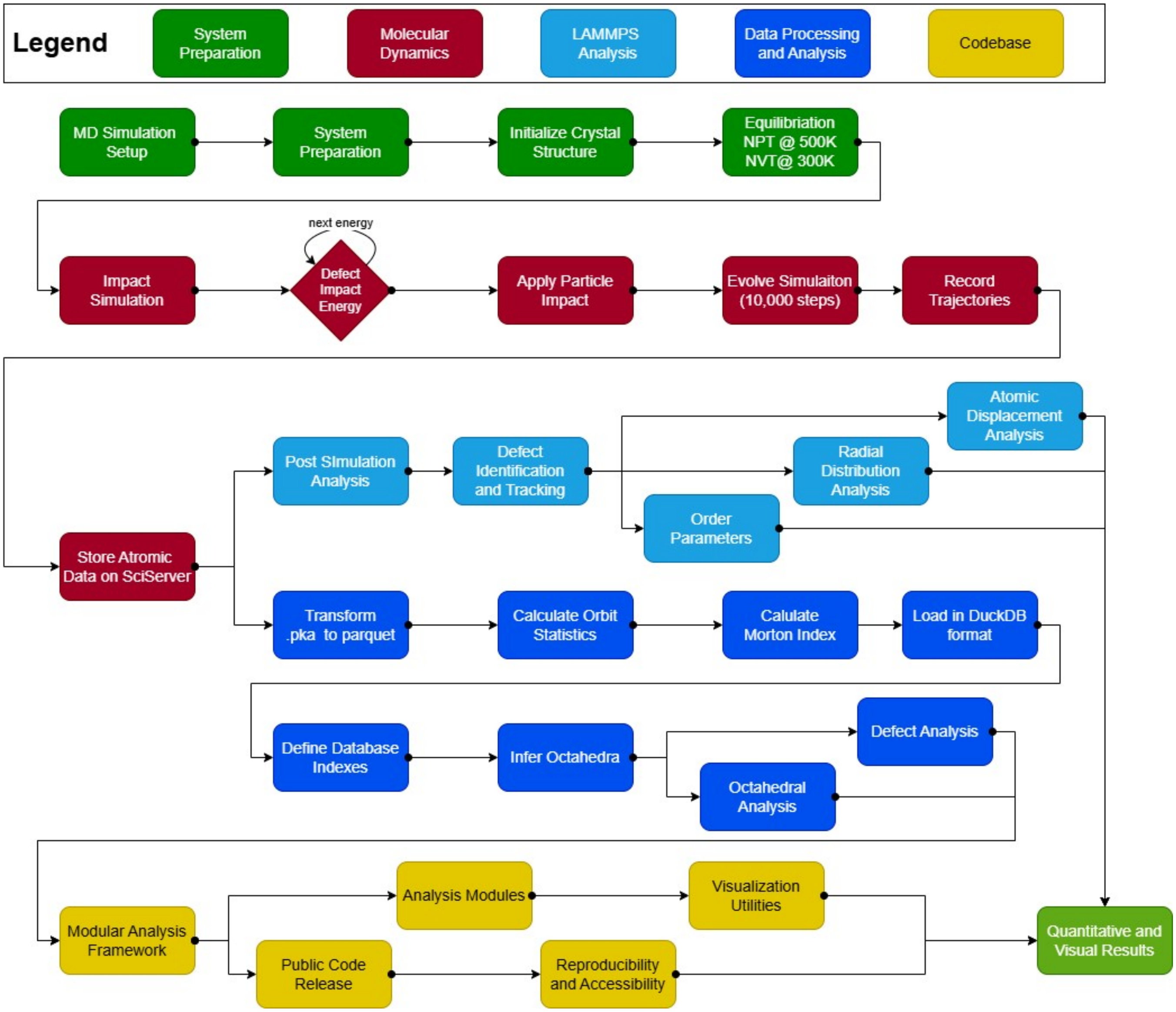

FIG. 1. Workflow for energetic particle impact simulations and analysis in halide perovskites. Nodes are color-coded by category as follows: green (System Preparation), dark red (Molecular Dynamics), light blue (LAMMPS Analysis), dark blue (Data Processing and Analysis), and yellow (Codebase). Large-scale LAMMPS/ReaxFF molecular dynamics simulations generate atomic trajectories under a range of primary knock-on atom (PKA) energies. Trajectory data are ingested into a structured SQL database, enabling reproducible analysis of defect formation, octahedral tilts (θ) and rotations (ϕ), Steinhardt order parameters (Q_4, Q_6), and species mobility (MSD), as well as spatial defect mapping. All analysis modules interface directly with SQL queries, allowing streamlined figure generation and transparent reproducibility through open-source scripts and databases.

we computed time-averaged positions, variances along each spatial direction, and the volume of the bounding box enclosing the full orbit. These quantities facilitate identification of atoms with large displacements and are stored for reuse. All calculations account for periodic boundary conditions in the $x-$ and $y-$ directions.

A central component of the analysis concerns the disposition of octahedral core structures, consisting of a type 2 (B) atom surrounded by six type 3 (X) atoms. Octahedra were identified every fifth simulation snapshot and stored as database tables for subsequent analysis. Identifying these structures requires, for each type 2 atom, finding its six nearest type 3 neighbors—a potentially expensive operation if implemented naively.

To accelerate these neighbor searches, we assign each atom a *z-index* identifying the grid cell it occupies in a 32^3 spatial grid spanning the simulation domain. For a given type 2 atom, candidate neighbors need only be searched within its own cell and the 26 adjacent cells. An index on the *z-index* column enables these queries to be executed efficiently, reducing overall query time by orders of magnitude. The grid cells are indexed using a Morton (z-order) space-filling curve, which provides

View Article Online
DOI: 10.1039/D6TA01465H

Open Access Article. Published on 15 June 2026. Downloaded on 6/17/2026 5:59:14 AM.
This article is licensed under a Creative Commons Attribution-NonCommercial 3.0 Unported Licence.

Journal of Materials Chemistry A Accepted Manuscript

an efficient one-dimensional mapping of three-dimensional space.

D. Analysis Using DuckDB

A central methodological innovation of this work is the development of a Structured Query Language (SQL)-based framework for MD trajectory post-processing. While most prior LAMMPS analyses rely on custom Python scripts or in-memory array parsing, here, we introduce a relational database architecture in which raw trajectory data are ingested into SQL tables and queried directly using DuckDB. Each simulation step is represented as a frame-specific entry, with individual atoms stored as records indexed by unique identifiers, species type, and temporal step. This design transforms trajectory analysis into a series of declarative SQL queries, allowing for efficient, reproducible, and scalable investigation of the complex atomic-scale phenomena at play.

This design transforms trajectory analysis into a series of declarative SQL queries, allowing the efficient retrieval of defect topologies, lattice distortions, and atomic trajectories through relational joins and indexed lookups. For instance, octahedral tilt distributions can be extracted via neighbor queries on Pb–X (X = halide) coordination polyhedra, while defect diffusion pathways are reconstructed by joining displacement data across sequential frames. Compared to conventional parsing, the SQL-based workflow provides significant improvements in efficiency, reproducibility, and modularity. Moreover, the approach naturally scales to the terabyte-sized datasets generated in radiation-damage simulations.

Our approach was critical to perform the specific analyses referenced in our workflow (Fig. 1). For instance, quantifying species-specific damage (Fig. 2) was accomplished by joining tables of atomic positions from before and after the impact event. Atomic displacements were computed as the Euclidean distance between pre-impact and post-impact coordinates following re-equilibration. Atoms were classified as “displaced” if their net displacement exceeded 2.0 Å , approximately half the Pb–I bond length and significantly larger than thermal vibrational amplitudes at 300 K.

A simple SQL query could then filter atoms exceeding this threshold and group the results by species, allowing efficient counting of displaced Cs, Pb, and I atoms at each impact energy.

Operationally, these displaced atoms serve as proxies for point defect formation. In particular, large displacements typically correspond to vacancy–interstitial (Frenkel) pairs, wherein the original lattice site becomes vacant and the displaced atom occupies a non-lattice position. To assess the possibility of anti-site defects (*i.e.,* a lattice site vacated by one species and subsequently occupied by a different species), we additionally examined the identities of nearest neighbor species relative to the reference lattice. Such events were rare within our displacement criterion and did not contribute significantly to the defect populations reported in Fig. 2

Furthermore, our primary analysis of the octahedral network distortions was conducted almost entirely within the SQL environment. To quantify the out-of-plane tilting (θ) and in-plane rotation (ϕ) of the PbI_6 octahedra, we executed queries that first identified the six nearest iodine neighbors for each lead atom (leveraging the indexed search described in Sec. II-C) and then performed trigonometric calculations on their coordinates directly within the query. This allowed us to extract angular distributions and map the landscape of structural disorder across hundreds of thousands of atoms and thousands of time steps.

Finally, reconstructing the dynamics of defect diffusion and self-healing was achieved by joining atomic data across sequential frames. By querying an atom's trajectory over time, we could analyze its displacement pathway and determine whether it returned to a stable lattice site. Compared to conventional parsing, SQL-based workflows provide significant improvements in efficiency and modularity. It establishes a quantitative and extensible framework for evaluating radiation hardness, which we anticipate can be generalized for the broader computational materials community.

E. Dissemination of Data and Code

The data that are produced and analyzed in this project are publicly available on the SciServer platform.[41] We store the original data products from the simulation as well as all the results produced by the post-processing pipeline. These data sets can be accessed from within compute containers that have all required libraries pre-installed.

All scripts, documentation, and schema definitions are also available in a public github repository.[42] By making the ingestion and analysis modules transparent, we provide the community with a reproducible, extensible, and high-throughput paradigm for trajectory analysis. To the best of our knowledge, this represents the first systematic use of SQL as a primary analytical back-end for post-processing LAMMPS trajectories in materials research. We anticipate that the framework we have provided can serve as a generalizable tool for the broader computational materials community, enabling efficient exploration of irradiation effects, defect dynamics, and structural transformations across a wide variety of systems.

This information will allow researchers to be able to adapt the code base for diverse material systems or extend the analysis with minimal reconfiguration. Importantly, the workflow is system-agnostic and not restricted to perovskites; any material simulated in LAMMPS can be incorporated in this code base, provided trajectory dumps are available.

III. RESULTS

We begin by quantifying which species are most labile as a function of PKA energy (Fig. 2). We observed that displaced iodine atoms dominate the defect population at low–to–moderate energies and remain the earliest species to respond to the impact. Above ∼300–500 eV, we observe a marked rise in Cs displacements (consistent with its lighter

View Article Online
DOI: 10.1039/D6TA01465H

Open Access Article. Published on 15 June 2026. Downloaded on 6/17/2026 5:59:14 AM.
This article is licensed under a Creative Commons Attribution-NonCommercial 3.0 Unported Licence.

mass and low A-site coordination). Pb atoms remain comparatively resilient across the impact energy range studied. This motivated the tilt/rotation analysis centered on the PbI_6 network that we undertook, and sets the stage for the impact depth and recovery results described below.

The primary goal of this study is to connect atomic-scale radiation damage events in $CsPbI_3$ with the ensuing structural distortions of the PbX_6 octahedral network (here, PbI_6) characteristic of MHP materials, where X represents a halide. While conventional defect-counting approaches can provide a first estimate of damage severity, they do not capture the continuous geometrical disorder introduced into the lattice. To address this gap, we quantify angular distortions in the Pb–I coordination environment using two complementary metrics: (i) an out-of-plane angle, θ, which measures the degree of octahedral tilting away from a perfect 180°, and (ii) an in-plane angle, ϕ, which tracks the rotation of iodide positions in the *xy* plane relative to the central Pb atom.

These angular metrics can be directly connected to established descriptions of perovskite structural instabilities, such as the Glazer tilt formalism.[43,44] Recent work has also established quantitative descriptors for analyzing these complex structural dynamics and octahedral distortions in metal halide perovskites[45]. As will be described in more detail below, our analysis demonstrates that halide disorder, manifested as both tilting (θ) and rotational (ϕ) disorder, is activated by primary knock-on atom (PKA) events, and that the magnitude of the disorder depends on the specific iodine site perturbed.

While our angular analysis focuses on the PbI_6 octahedra, our broader defect analysis framework comprehensively tracks the displacement of *all* atomic species, including Cs and Pb, providing a complete picture of the radiation-induced disorder. Importantly, this approach reveals not only where defects are created, but also how the surrounding lattice accommodates them through angular distortions. By combining defect-counting with angular distribution analyses, we are able to obtain a comprehensive picture of the local landscape of the resulting structural damage. This framework will be critical for assessing the extent to which dynamic self-healing mechanisms can recover the crystalline order after irradiation.

The questions we ask in the following sub-sections cover these questions:

1. **Structural damage:** What is the energy threshold for widespread post-impact disorder? And to what extent is that disorder repaired after 10 *ps*?

2. **Identity of displaced particles:** Which atom-type(s) (Cs, the A-site cation, Pb, the B-site cation, and I anions) are significantly displaced (*i.e.,* moved from their original octahedron, whether transiently or permanently) at a given incident energy of the energetic particle)? And how many of each atom-type is affected by the damage?

3. **Extent of damage:** How far does the damage extend before annealing? And what are the extant mechanisms by which the lattice accommodates the imparted energy?

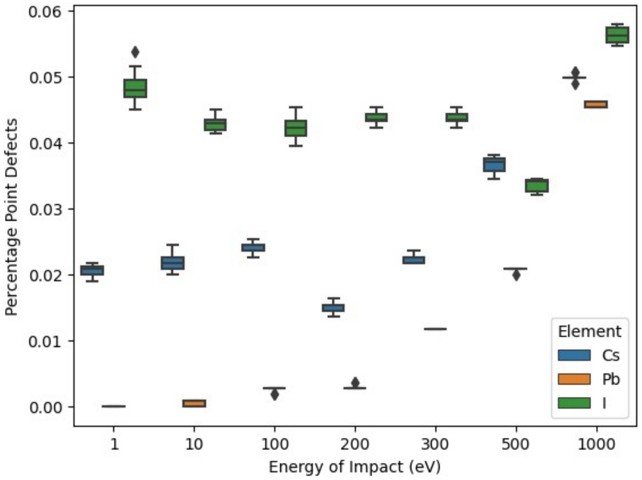

FIG. 2. Percentage of point defects created as the energy of the impact increases, shown for the different types of atoms in the system: Iodine atoms are the most mobile at all energies. Cs atoms are significantly affected after about 300 eV. Pb atoms are the most resilient to the energy influx. They begin to show the influence of the energy input after about 300 eV, after which the incidence of defective Pb atoms rises quite quickly. The narrow colored areas are provided as a guide to the eye.

4. **Self-healing:** To what extent do the lattices self-heal after 10 *ps* and what defects remain?

A. Steinhardt Order Parameters

Steinhardt order parameters have been widely used to characterize the local orientational order in atomic or molecular systems.[46] They are defined as follows:

$$q_l(i) = \left(\frac{4\pi}{2l+1} \sum_{m=-l}^{l} |q_{lm}(i)|^2 \right)^{1/2} \tag{1}$$

where

$$q_{lm}(i) = \frac{1}{N(i)} \sum_{j=1}^{N(i)} Y_{lm}(\mathbf{r}_{ij}) \tag{2}$$

Here, Y_{lm} denotes spherical harmonics, $N(i)$ is the number of neighboring atoms of atom i, $\mathbf{r}_{ij}$ is the vector connecting atom i to its neighbor j, l is a non-negative integer that determines the symmetry being probed, m takes integer values from $-l$ to l. Values of $q_l(i)$ serve as fingerprints of local structural order. For the calculation, the first nearest-neighbor shell is typically considered, and the cutoff radius may vary depending on the lattice type.

We compute local bond-orientational order parameters q_ℓ following Steinhardt *et al.*, using $\ell = 4, 6$ to distinguish perovskite-like order from disordered regions. We are interested in looking at the PbI_6 octahedra and, to that end, we calculated the radial distribution plot (Figure 3) for estimation

Journal of Materials Chemistry A Accepted Manuscript

View Article Online
DOI: 10.1039/D6TA01465H

Open Access Article. Published on 15 June 2026. Downloaded on 6/17/2026 5:59:14 AM.
This article is licensed under a Creative Commons Attribution-NonCommercial 3.0 Unported Licence.

Journal of Materials Chemistry A Accepted Manuscript

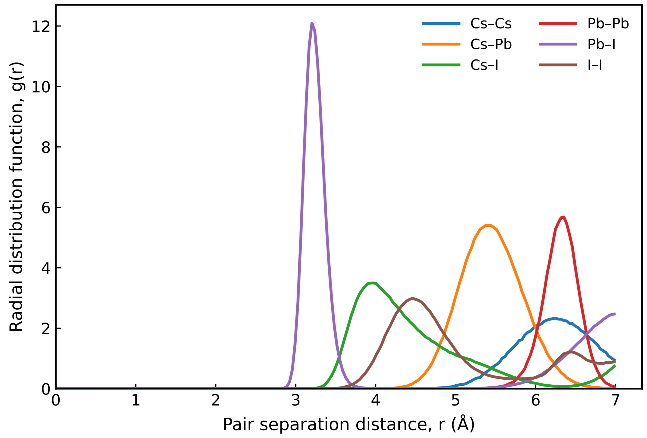

FIG. 3. Pairwise radial distribution functions g(r) for Cs–Cs, Cs–Pb, Cs–I, Pb–Pb, Pb–I, and I–I atomic pairs in $CsPbI_3$, computed from equilibrated molecular dynamics trajectories. The RDFs quantify short- and medium-range structural order of the perovskite lattice via the probability of finding a pair of atoms separated by a distance r relative to an ideal gas at the same density. Sharp first-neighbor peaks for Pb–I and I–I pairs reflect the integrity of the corner-sharing PbI_6 octahedral framework, while broader features at larger r indicate longer-range lattice correlations. Cs-containing pair distributions exhibit broader and lower-amplitude peaks, consistent with the more weakly bound and spatially diffuse nature of the A-site cations. Together, these RDFs establish a structural baseline for the crystalline perovskite lattice against which radiation-induced disorder and post-impact structural recovery are assessed in subsequent analyses.

of the cut-offs for the calculation of the order parameters. We chose the first nearest neighbor shell as the cut-off distance in order to calculate the Steinhardt order parameters. Neighbors are defined within a 3.7 Å cut-off around each Pb atom. In pristine $CsPbI_3$, the Pb exhibits Steinhardt values $q_4 \approx 0.76$ & $q_6 \approx 0.35$. The effect of the impact reduces both q_4 and q_6 values within the cascade zone. The sharp first-neighbor Pb–I peak in Figure 3, centered at ≈3.2 Å, serves as the pristine bond length reference against which radiation-induced structural distortions are assessed throughout this work; broadening and asymmetry of this peak at higher impact energies confirm that radiation damage predominantly drives bond-angle and bond-length disorder within the octahedral framework, while direct bond-breaking events occur at comparatively lower frequencies. Although less common, these bond-breaking events may still contribute to defect formation and electronic trap states that influence charge transport behavior. This is consistent with the angular analyses presented in Sections III.C and III.D.[20]

Figure 2 quantifies the percentage of defects by atom-type (Cs, Pb, I) across the energy range studied, whereas Fig. 4 presents the evolution of Steinhardt order parameters, providing a complementary measure of structural disorder.

To provide a quantitative characterization of local orientational disorder induced by a high energy collision, we computed the Steinhardt bond orientational order parameters, q_4 and q_6, for Pb atoms using their surrounding I neighbors, thereby probing distortions of the PbI_6 octahedra. The analysis was restricted to a localized region centered on the impact site for the 1000 eV primary knock-on atom (PKA) event, allowing the structural response of the most strongly perturbed volume to be isolated from the largely undisturbed bulk lattice.

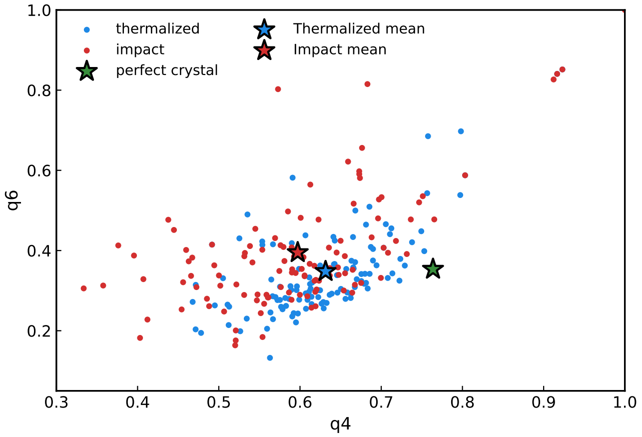

FIG. 4. Steinhardt order parameters q_4 and q_6 for Pb in the central region surrounding the impact site following a 1000 eV primary knock-on atom (PKA) event in $CsPbI_3$. Values are shown for the thermally equilibrated lattice prior to impact and for the post-impact configuration. Faint scattered points correspond to instantaneous q_4 and q_6 values of individual atoms. Larger symbols denote the corresponding ensemble-averaged values within the analyzed region. The pre-impact distribution clusters near values characteristic of a crystalline perovskite environment, whereas post-impact data exhibit a clear shift towards lower q_4 and q_6, accompanied by a substantial broadening of the distributions. The average q_6 value decreases from its thermalized value by a few tenths, indicating a marked loss of local orientational order consistent with radiation-induced lattice disorder near the impact zone. Deviation from the reference values for a perfect lattice, shown for comparison, highlights that the structural response is highly localized and reflects partial, rather than complete, loss of crystalline order. This drift in Steinhardt parameters provides a quantitative measure of the degree of local structural disruption induced by high-energy particle impact.

Before discussing the impact-induced changes, we first establish the physical interpretation of q_4 and q_6 in the context of the perovskite octahedral framework. The q_4 order parameter is directly sensitive to four-fold rotational symmetry: for a perfect, undistorted PbI_6 octahedron with O_h point symmetry, q_4 attains its maximum value of ≈ 0.764, reflecting the ideal arrangement of I–Pb–I bond angles at exactly 90° and 180°.[46] Any departure from this geometry, whether through I–Pb–I bond angle distortion, octahedral tilting, or halide displacement, reduces the local four-fold symmetry and decreases q_4. A decrease in q_4 is therefore a direct, quantitative measure of angular deviation from ideal octahedral coordination and serves as a sensitive indicator of radiation-induced distortion of the PbI_6 framework.

The q_6 order parameter captures orientational correlations projected onto $l = 6$ spherical harmonics, which are sensitive to lower-symmetry structural arrangements. For an ideal undistorted octahedron, $q_6 \approx 0.354$. When octahedra undergo

View Article Online
DOI: 10.1039/D6TA01465H

Open Access Article. Published on 15 June 2026. Downloaded on 6/17/2026 5:59:14 AM.
This article is licensed under a Creative Commons Attribution-NonCommercial 3.0 Unported Licence.

Journal of Materials Chemistry A Accepted Manuscript

collective tilting or in-plane rotation, as occurs in the Glazer tilt systems that characterize structural phase transitions in perovskites,[43,44] the distribution of halide positions around each Pb center develops angular character that projects preferentially onto $l = 6$ harmonics, causing q_6 to increase above its ideal octahedral value. An increase in q_6 following impact therefore does not indicate enhanced crystallinity; rather, it signals the activation of collective tilt and rotation modes of the PbI_6 network. This interpretation is consistent with recent work by Liang *et al.*,[45] who demonstrated that q_6 serves as a sensitive descriptor of dynamic octahedral tilting in metal halide perovskites, and with the direct angular analysis of tilt (θ) and rotation (ϕ) distributions presented in subsequent sections of this manuscript. Taken together, the coupled decrease in q_4 and increase in q_6 thus constitute a coherent, symmetry-grounded signature of radiation-induced octahedral distortion: the former quantifies the loss of ideal bond-angle geometry within individual octahedra, while the latter reflects the onset of collective tilting and rotational disorder across the network.

In the thermally equilibrated lattice prior to impact, average values of q_4 and q_6 are 0.63 and 0.35, respectively, compared to reference values of 0.76 (q_4) and 0.35 (q_6) for an ideal, undistorted octahedral environment. The reduction in q_4 relative to the perfect structure reflects finite temperature angular fluctuations and an intrinsic lattice "softness" inherent to the perovskite framework. Following the 1000 eV impact, the average value of q_4 decreases further to 0.59, corresponding to an additional reduction of approximately 6.3% relative to the thermalized state and a total reduction of about 22.8% relative to the perfect lattice. This decrease directly indicates enhanced angular distortion of the PbI_6 octahedra, with I–Pb–I bond angles deviating increasingly from their ideal values, which should be 180°.

In contrast, q_6 increases from 0.35 in the thermalized configuration to 0.39 after impact, representing an increase of approximately 11.4% relative to the thermalized state. This increase does not signify enhanced crystallinity, but rather reflects a redistribution of orientational correlations associated with collective distortions of the octahedral network, such as tilting and rotation of PbI_6 units. The substantial broadening of q_4 and q_6 distributions at the atomic level, evident from the scattered per-atom values, further highlights the heterogeneous nature of post-impact local environments.

Taken together, the coupled decrease in q_4 and concomitant increase in q_6 demonstrates that the 1000 eV impact induces strong, localized orientational disorder while preserving a degree of short-range structural coherence. These results indicate that radiation damage in $CsPbI_3$ is dominated by distortions of the octahedral framework rather than complete loss of local coordination, providing a quantitative structural basis for the defect-tolerance and partial recovery behavior discussed in subsequent sections.

Figures 5 and 6 illustrate the spatial distribution of structural defects identified after irradiation events at different PKA energies. Defects are registered at the centers of octahedra within which at least one iodine atom has been displaced relative to the pristine lattice. We chose the iodine atom as the minimum marker for structural disorder because they are the most labile of the atoms in the system, not unexpectedly.

At high energy (1,000 eV, Fig. 5), the cascade extends deeply into the simulation cell, generating a broad region of amorphization. In contrast, at low energy (1 eV, Fig. 6), defect creation is shallow and localized near the impact site, with the majority of the bulk lattice remaining crystalline.

These projections clearly demonstrate and quantify the depth-dependence of impact damage. Using the Pb-Pb nearest-neighbor distance of 6.3 Å from the radial distribution function (Figure 3) as a structural ruler, we can gauge the true extent of these cascades. The deep damage zone at 1000 eV (Figure 5) extends approximately 150 Å into the bulk, corresponding to a penetration depth of roughly 24 unit cells. In contrast, the 1 eV impact (Figure 6) is confined to the immediate surface layer, affecting only the first 1-2 octahedral layers. This scaling confirms that high-energy impacts do not merely perturb the surface but drive structural disorder deep into the crystallographic bulk. In particular, the *xy*, *xz*, and *yz* views confirm that higher-energy PKA events produce not only a higher density of disrupted octahedra but also deeper penetration of the cascade front into the bulk. This spatial mapping provides a high-level "big picture" of the damage profile, which we then connect to local geometrical distortions using the angular analyses below.

B. Octahedral spinning

To move beyond simply counting the number of point defects and, instead, directly interrogate the dynamical response of the octahedral framework, we analyzed the cumulative rotational activity of PbI_6 octahedra following impact events across a wide range of incident energies (Fig. 8). This analysis captures collective lattice dynamics by tracking changes in the angular indices of iodide sites surrounding each Pb center, thereby providing a spatially resolved measure of octahedral rotation and reorientation induced by the collision cascade.

At low impact energies (1–10 eV), rotational activity remains weak and highly localized near the surface, indicating that the lattice accommodates the imparted energy primarily through small-amplitude angular fluctuations. As the impact energy increases ($\geq$100 eV), pronounced rotational activity emerges at the impact site and propagates progressively deeper into the bulk. At the highest energies studied (500–1000 eV), extended regions of intense octahedral rotation are observed, forming a contiguous subsurface zone of dynamic angular disorder. The depth and lateral spread of this rotational activity closely mirror the penetration depth of the collision cascade inferred from defect density maps (Fig. 5), demonstrating that angular reorientation of the octahedral network is an intrinsic component of radiation damage propagation.

Importantly, these cumulative rotation maps reveal that radiation-induced disorder in metal halide perovskites is not limited to atomic displacements or coordination defects. Instead, a significant fraction of the deposited energy is absorbed through *collective* rotational excitations of the PbI_6 framework, which persist over thousands of timesteps follow-

View Article Online
DOI: 10.1039/D6TA01465H

Open Access Article. Published on 15 June 2026. Downloaded on 6/17/2026 5:59:14 AM.
This article is licensed under a Creative Commons Attribution-NonCommercial 3.0 Unported Licence.

Journal of Materials Chemistry A Accepted Manuscript

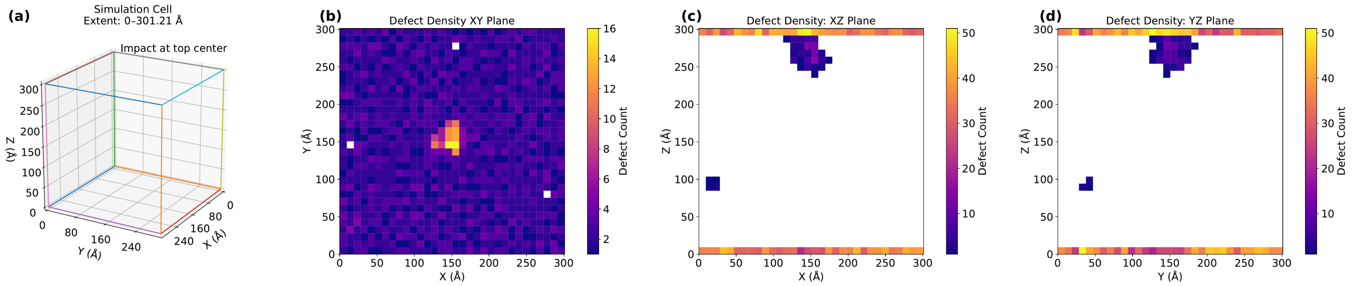

FIG. 5. Spatial distribution of structural defects in the perovskite lattice following a simulated impact event at 1 *keV*. (a) Schematic of the simulation cell showing its full extent (0–301.21 Å) and the location of the impact site at the top center of the *z*-axis; this panel serves as a geometric orientation guide for the heat maps shown in panels (b)–(d). (b)–(d) Two-dimensional heat maps showing the defect density projected onto the *x*-*y*, *x*-*z*, and *y*-*z* planes of the simulation cell, respectively. The data correspond to a snapshot taken at 20,000 *fs* from a simulation initiated by a 1 keV Primary Knock-on Atom (PKA) event. A structural defect is registered at the center of any octahedron where the identity of at least one corner atom has changed relative to the initial perfect crystal structure. The color intensity scale represents the number of identified defect centers per spatial bin; the simulation box is divided into 32×32 bins, with each bin represented by one pixel. The figure clearly portrays the extent of structural damage and the localized regions of amorphization resulting from the 1 keV impact.

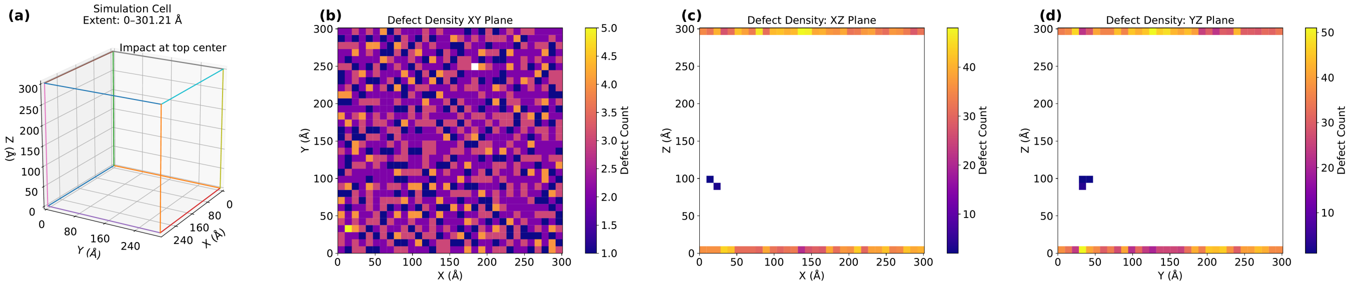

FIG. 6. Spatial distribution of structural defects in the perovskite lattice following a simulated impact event at 1 *eV*. (a) Schematic of the simulation cell showing its full extent (0–301.21 Å) and the location of the impact site at the top center of the *z*-axis; this panel serves as a geometric orientation guide for the heat maps shown in panels (b)–(d). (b)–(d) Two-dimensional heat maps showing the defect density projected onto the *x*-*y*, *x*-*z*, and *y*-*z* planes of the simulation cell, respectively. The data correspond to a snapshot taken at 20,000 *fs* from a simulation initiated by a 1 eV Primary Knock-on Atom (PKA) event. the same defect registration and binning conventions apply as in Figure 5. At 1 eV, defects remain localized within ∼2 nm of the surface with minimal penetration into the bulk, in stark contrast to the extended cascade produced by the 1000 eV impact shown in Figure 5. The majority of the lattice retains its crystalline order across all three projections.

ing impact. The spatial coherence of these rotational patterns suggests that octahedral tilting and rotation serve as an efficient channel for redistributing kinetic energy away from the primary impact site, consistent with the intrinsic lattice softness of perovskite materials.

Motivated by the pronounced rotational activity observed in these maps, we quantified how this dynamically perturbed region manifests itself in terms of local orientational order. Specifically, we evaluated the Steinhardt bond orientational order parameters q_4 and q_6 for Pb atoms within the rotationally active zone identified in Fig. 4. This targeted analysis allows a direct connection to be drawn between spatially resolved octahedral dynamics and quantitative measures of local structural order. As discussed in the previous section, the observed drift in q_4 and q_6 values reflects the cumulative effect of sustained octahedral rotation and tilting, rather than complete loss of coordination, reinforcing the picture that radiation damage in these systems is dominated by heterogeneous angular disorder within an otherwise connected octahedral network.

C. Octahedral Tilt Disorder: θ Angle Distributions

Figure 9 presents the distribution of θ angles for octahedra altered by the impact, defined as those octahedra in which at least one iodine atom is different from the six original iodine atoms that initially formed the octahedron. In the undistorted perovskite lattice, Pb–I–Pb linkages within the Pb-centered octahedra are expected to remain close to linearity, with $\theta \approx 180^\circ$ for apical iodides and $\theta \approx 90^\circ$ for equatorial linkages. See Fig S.2 for a schematic diagram of an octahedral. Radiation-induced displacements broaden these distributions substantially, with distinct differences observed across the six iodide indices (cindex 1–6). In particular, distortions are more pronounced at apical sites (cindex 1 and 6), indicating a higher susceptibility of axial bonds to knock-on events. This broadening directly reflects the increase in octahedral tilt disorder following impact.

Table I summarizes the statistics we observed for the tilt angle, θ, across the impact energies studied. At 1 eV, the median θ remains close to its ideal value, averaging at 178° with a narrow spread of ±5°. In contrast, at 1,000 eV, the distribu-

View Article Online
DOI: 10.1039/D6TA01465H

Open Access Article. Published on 15 June 2026. Downloaded on 6/17/2026 5:59:14 AM.
This article is licensed under a Creative Commons Attribution-NonCommercial 3.0 Unported Licence.

tion broadens considerably, ranging between 120–180°, with a median near 150°. Apical iodides (index 1 and 6) exhibit up to 40° larger deviations than equatorial sites.

TABLE I. Statistical measures of θ distributions for octahedra that were changed as a result of different PKA energies.

Energy (eV)	Median θ (°)	Range (°)	Std. Dev. (°)	Most affected sites
1	178	170–180	3	None significant
10	170	150–180	8	Equatorial
100	170	150–180	8	Equatorial
200	170	150–180	8	Equatorial
500	160	130–180	15	Apical (1,6)
1000	150	120–180	18	Apical (1,6)

D. Octahedral Rotational Disorder: ϕ Angle Distributions

Complementary insight is obtained from a study of the rotational, ϕ, angle distributions shown in Figure 10. Here, ϕ denotes the azimuthal orientation of Pb–I bonds in the *xy* plane, and thus encodes the rotational modes of the PbI_6 octahedra. In the pristine lattice, iodine atoms adopt well-defined orientations consistent with the high-symmetry cubic perovskite phase. Under irradiation, however, the ϕ distributions broaden and shift, signaling in-plane torsions and rotations of the octahedra. Together with the θ distributions, these results highlight that radiation damage is not limited to point-defect creation but also drives collective and concerted tilts and rotations of the octahedral framework.

Table II provides quantitative measures of ϕ. At 1 eV, ϕ is narrowly distributed around 0° and 90°, whereas at 1,000 eV the spread reaches ±100°, reflecting significant torsional rotations.

TABLE II. Statistical measures of ϕ distributions for octahedra that were changed as a result of different PKA energies.

Energy (eV)	Median ϕ (°)	Range (°)	Std. Dev. (°)
1	0/90	±10	5
10	15/95	±25	12
500	30/110	±60	28
1000	45/120	±100	40

E. Connecting Spatial and Angular Metrics

By combining defect density maps with angular distribution analyses, we can obtain a more holistic picture of the radiation damage process. Spatial projections (Figs. 5–6) quantify the extent and depth of the cascade, while the θ and ϕ distributions (Figs. 9–10) reveal the local geometric response of the lattice to these impacts.

At 1000 eV, θ broadens by nearly 60° and ϕ by $\sim$100°, whereas, at 1 eV, the broadening remains below 10° for both metrics. This quantitative link demonstrates that cascade penetration depth (Figs. 5–6) directly correlates with the magnitude of the angular disorder.

A direct connection can be drawn between the angular disorder observed in our simulations and the classical classification of tilt systems by Glazer.[43] In Glazer's scheme, static octahedral tilts are described by combinations of rotations about the pseudo-cubic axes, leading to well-defined symmetry-lowering distortions, such as $a^-a^-a^-$ (rhombohedral) or $a^0a^0c^-$ (tetragonal). In contrast, the radiation-induced distortions captured in our θ and ϕ distributions represent a dynamically broadened analog of these tilted systems. For instance, the broad spread of θ angles around the apical sites (cindex 1 and 6, Fig. 9) resembles local activation of out-of-phase a^- tilts about the $c-$ axis, whereas the in-plane torsions observed in the ϕ distributions (Fig. 10) mimic the onset of rotations akin to $a^0a^0c^-$ modes. Unlike equilibrium tilt transitions, however, our results demonstrate that such tilt-like distortions can be nucleated transiently by high-energy particle impacts, with their magnitude and spatial extent scaling with PKA energy (Figs. 5–6). This correspondence highlights the fact that radiation damage drives perovskites into dynamically fluctuating tilt configurations comparable to those that define their thermodynamic polymorphs, thereby providing a structural framework for interpreting disorder within the language of Glazer tilt notation.

A compelling link can be established between our simulation results and the classical Glazer classification of octahedral tilt systems.[43] In Glazer's foundational work, specific notations (such as $a^0a^0c^-$) are used to describe the static, cooperative rotations that define stable perovskite phases. In contrast, our findings reveal that high-energy particle impacts can transiently nucleate similar distortions in a dynamic, non-equilibrium fashion. For instance, the pronounced angular spread at apical sites (Fig. 9) is effectively a localized, dynamic activation of out-of-phase tilts. This correspondence is significant because it allows us to interpret the complex, fluctuating disorder created by radiation damage using the robust and well-understood language of Glazer tilts. It suggests that the structural pathways for radiation damage and for thermodynamic phase transitions are fundamentally linked.

A useful point of comparison comes from experimental measurements of octahedral distortions in $CsPbI_3$ nanocrystals.[24] Matuhina *et al.* systematically tuned the reaction temperature of $CsPbI_3$ nanocrystals and reported that the most phase-stable samples (NCs synthesized at 150 °C) exhibited the lowest octahedral distortion, with refined Pb–I–Pb bond angles clustering around ~160° in the cubic perovskite phase. This experimentally measured angular range aligns closely with the distributions obtained in our simulations, We observe a significant density of rotations near 155–165°. The agreement suggests that the types of shallow, thermally accessible, tilts governing phase stability in nanocrystals are similar in magnitude to the small, spatially extended distortions induced in our slab geometry by low-energy irradiation. In other words, our MD results reproduce the same characteristic octahedral bending that experimental studies have identified as being intrinsic to $CsPbI_3$'s structural softness and phase behavior. This provides additional confidence that the angular disorder captured in our trajectories is physically realistic and consistent with known experimental benchmarks.

Journal of Materials Chemistry A Accepted Manuscript

Open Access Article. Published on 15 June 2026. Downloaded on 6/17/2026 5:59:14 AM.
This article is licensed under a Creative Commons Attribution-NonCommercial 3.0 Unported Licence.

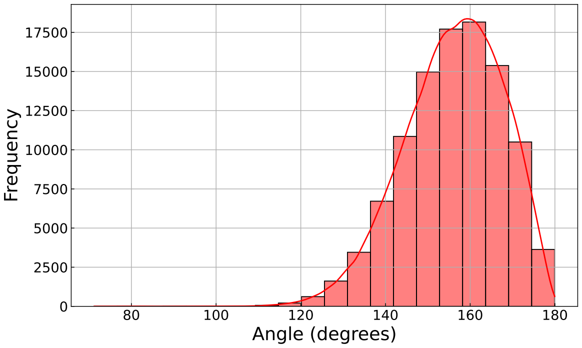

FIG. 7. Distribution of Pb–I–Pb bond angles in $CsPbI_3$ following energetic particle impact at 1000 eV. The histogram shows the frequency of all Pb–I–Pb angles extracted from the MD trajectory at a chosen timestep, capturing both apical and equatorial linkages across the full lattice. In a pristine cubic perovskite phase, Pb–I–Pb angles should be exactly 180 °, reflecting the linear connectivity of the undistorted octahedral network. Following impact and thermal fluctuations, the distribution broadens significantly, with a pronounced population extending from 155° to 165°, indicating the onset of substantial octahedral tilting and bond-bending as the lattice accommodates the local temperature and localized energy deposition.

Figure 9 presents distributions of the octahedral tilt angle θ for PbI_6 octahedra that are structurally altered following irradiation. In a pristine cubic perovskite lattice, θ values are sharply clustered around well-defined angles corresponding to ideal octahedral geometry: $\theta \approx 180°$ for apical Pb–I bonds and $\theta \approx 90°$ for equatorial bonds (see Fig. S2 for a schematic definition of θ).

Following irradiation, these sharp angular peaks broaden substantially; however, the resulting distributions are not random. Instead, θ values remain strongly clustered around physically meaningful angles, indicating that the octahedra preferentially occupy metastable, tilted configurations rather than undergoing complete angular disorder. At low impact energies (1–10 eV), the θ distributions remain narrowly centered near their ideal values, with median deviations of less than ~10°.

At higher energies ($\geq$500 eV), the distributions broaden asymmetrically, particularly for the apical iodide sites (c-index 1 and 6), where θ values span approximately 120–180°, with clear maxima near 150–160°. These angles correspond to pronounced but continuous octahedral tilting, rather than bond breaking or amorphization. Equatorial sites (c-index 2–5) exhibit comparatively smaller deviations, remaining clustered near ~90° with moderate broadening.

The persistence of clustering around these characteristic angles demonstrates that radiation damage predominantly drives the lattice into distorted, yet topologically intact, octahedral configurations. This behavior highlights octahedral tilting as a primary structural accommodation mechanism by which $CsPbI_3$ absorbs and redistributes the imparted kinetic energy while preserving short-range connectivity.

F. Dynamics of Lattice Recovery

Finally, to quantify the overall ability of the lattice to self-heal following the collision cascade, we tracked the trajectories of all displaced atoms to determine if they returned to stable lattice sites. Figure 11 presents the recovery statistics for each species, defined as the fraction of displaced atoms returning to within 2 Å of a crystallographically equivalent site. We observe a strong species-dependence in this healing process: While the heavier cations (Cs and Pb) exhibit limited recovery (dropping to 4.5% and 8.7% respectively at 1000 eV), the iodide sublattice demonstrates a remarkable capacity for self-repair. Even with a 1000 eV impact, approximately 32% of all displaced iodine atoms recover to lattice sites within 10 *ps*. This suggests that the radiation tolerance of $CsPbI_3$ is driven by the high mobility of the halide network, which can efficiently annihilate vacancies and restore order even after high-energy perturbations.

These structural recovery statistics have direct implications for optoelectronic performance. The dominance of halide Frenkel pairs, with negligible anti-site formation (<1.5% for all species), is electronically favorable: First principles calculations have established that halide vacancies and interstitials in lead halide perovskites are electronically shallow, residing near the band edges rather than deep within the gap,[13] and are therefore unlikely to act as deep non-radiative recombination centers.[9] The octahedral tilting we observe does, in principle, affect the band structure, since deviations of Pb–I–Pb bond angles from 180° reduce *s*-*p* orbital overlap and widen the band gap.[19] However, at low impact energies (1–10 eV), the tilt deviations remain within ∼10° of the ideal value and, even at 1000 eV, the cascade zone constitutes a small fraction of the total device volume under realistic irradiation fluences. Structural recovery is a necessary but not sufficient condition for full functional recovery; the primary bottleneck is the limited self-healing of the Cs and Pb sublattices (<9% at 1000 eV), since unrecovered cation vacancies are more likely than halide Frenkel pairs to produce electronically active defect states. Experimental studies of perovskite solar cells under proton irradiation confirm partial but incomplete efficiency recovery at high fluences, consistent with this structural picture.[47,48] Future work combining these trajectories with calculations of defect electronic structure would provide a direct quantitative link between the recovery fractions reported here and device-level performance metrics.

IV. CONCLUSIONS

The combination of MD results analyzed using SQL provided a highly detailed and quantitative picture of the effect that an energetic particle imparts to a perfectly crystalline $CsPbI_3$ lattice. Together, these two techniques constitute a powerful tool that could be broadly applied to applications far from the one studied here.

From a qualitative standpoint, our results covering the effects of 1 to 1000 eV impacts showed that high-energy events generate broad angular disorder across multiple in-

Journal of Materials Chemistry A Accepted Manuscript

View Article Online
DOI: 10.1039/D6TA01465H

Open Access Article. Published on 15 June 2026. Downloaded on 6/17/2026 5:59:14 AM.
This article is licensed under a Creative Commons Attribution-NonCommercial 3.0 Unported Licence.

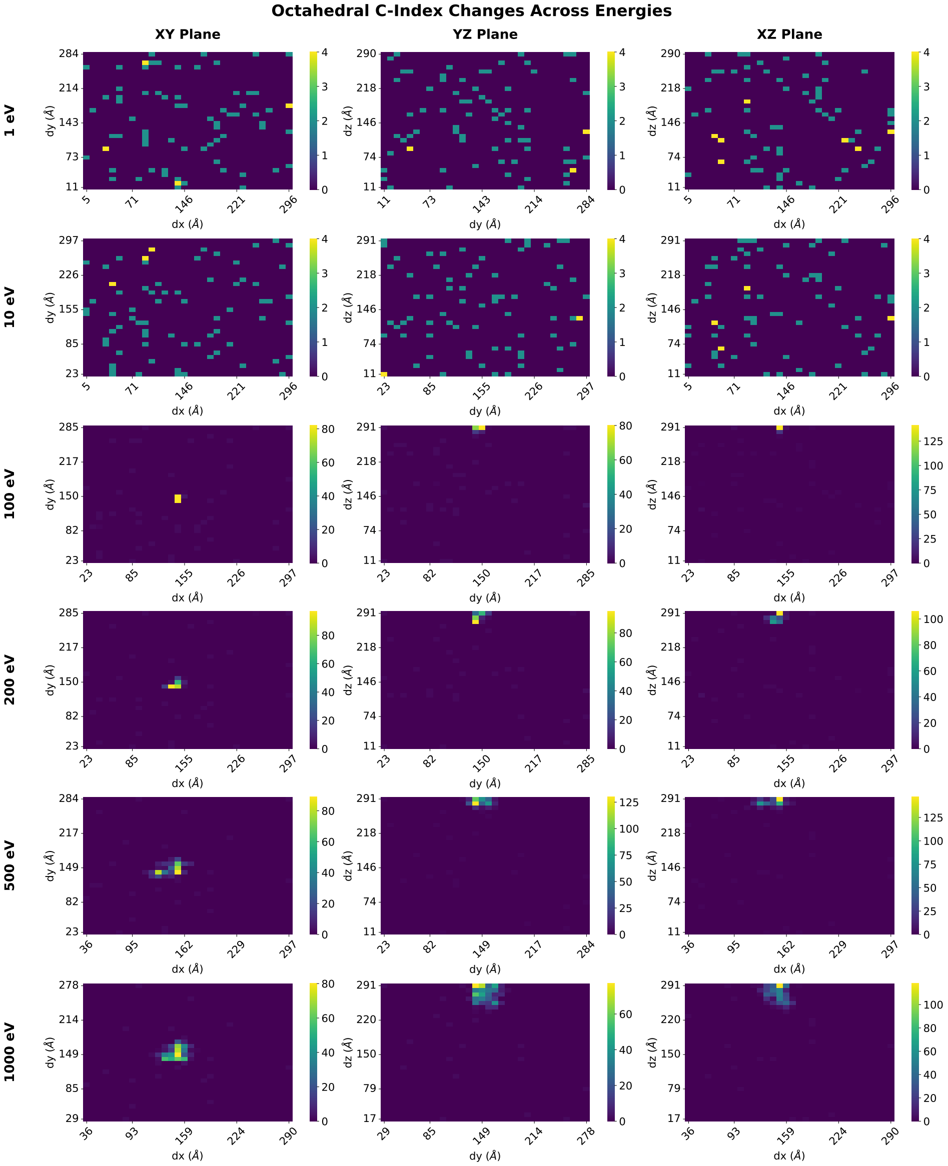

FIG. 8. Cumulative octahedral spin activity in $CsPbI_3$ under the influence of an energetic particle impact. Cumulative maps show the magnitude and spatial distribution of octahedral rotational dynamics as a function of impact energy (1–1000 eV). The quantity plotted here corresponds to the cumulative change in iodine atom site angular indices (c-index) for each PbI_6 octahedron, summed every 50 timesteps after impact and binned into a 32×32 grid. The resulting "heat maps" represent the cumulative rotational activity (or "spin") of the octahedra, revealing where and how strongly the lattice undergoes dynamic angular reorientation. As the impact energy increases, intense rotational activity emerges near the surface where the energetic particle strikes, with progressively deeper penetration into the bulk region. The spatial extent of this rotation correlates directly with the cascade depth observed in defect density maps (see Fig. 5). Note that color scales are independently normalized for each energy to highlight spatial variation rather than absolute magnitude. The analysis demonstrates that radiation-induced lattice dynamics involve not only atomic displacements but also collective rotational excitations of the octahedral network, with stronger and more spatially extended spin activity at higher energies.

dices, whereas low-energy events yield more localized and recoverable distortions. We showed that the halide atoms were most easily displaced from their original lattice sites. It took considerably more impact energy (above 300-500 eV) to displace the central Cs atoms, with Pb atoms generally resistant to displacement. Quantitative analysis of atomic displacements reveals a high degree of self-healing, particularly within the halide sublattice. As shown in Figure 11, the recovery mechanism is strongly species-dependent. At the highest impact energy of 1000 eV, while heavier Cs and Pb cations exhibit limited recovery (4.5% and 8.7% respectively), the iodine anions show a pronounced capacity for self-repair, with approximately 32% of all displaced atoms returning to crystallographically equivalent sites. Notably, despite the energetic disorder, our analysis of the relaxed configurations reveals negligible anti-site formation (<1.5% for all species),

Journal of Materials Chemistry A Accepted Manuscript

Open Access Article. Published on 15 June 2026. Downloaded on 6/17/2026 5:59:14 AM.
This article is licensed under a Creative Commons Attribution-NonCommercial 3.0 Unported Licence.

Journal of Materials Chemistry A Accepted Manuscript

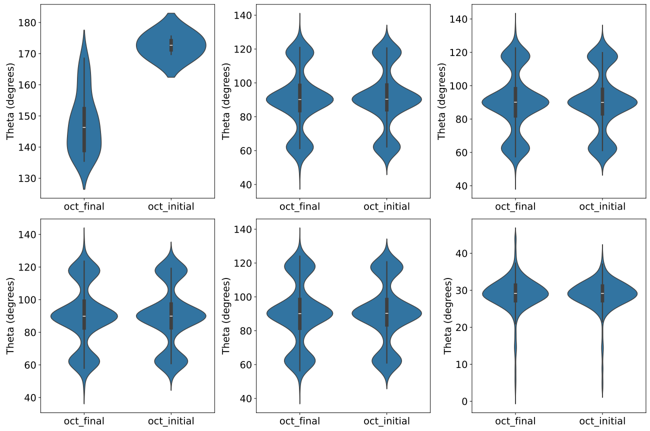

FIG. 9. Distribution of octahedral tilt angles (θ) for PbI_6 octahedra in $CsPbI_3$ that are structurally altered following a 1000 eV irradiation event. An octahedron is classified as “changed” if at least one iodine atom differs from its original coordination in the pristine lattice. Panels correspond to individual iodide sites (c-index 1–6), where c-index 1 and 6 denote apical iodides and c-index 2–5 correspond to equatorial iodides. In the ideal cubic perovskite structure, θ values cluster near 180° for apical bonds and 90° for equatorial bonds (see Fig. S2 for a schematic illustration). Following irradiation, the θ distributions broaden but remain clustered around these characteristic angles, indicating preferential occupation of metastable tilted configurations rather than complete angular disorder. Apical sites exhibit the largest deviations, with θ values extending toward ~150° at high impact energies, reflecting enhanced susceptibility of axial bonds to radiation-induced tilting.

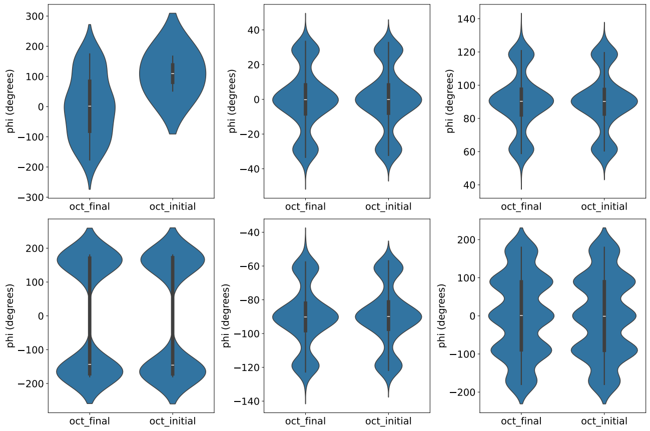

FIG. 10. Distribution of in-plane bond angles (ϕ) for *changed octahedra* in $CsPbI_3$ following irradiation. The ϕ angle is defined as the projection of the Pb–I bonds in the *xy* plane relative to the central Pb atom, capturing the rotational orientation of the six surrounding iodine atoms. Panels correspond to different iodine sites (c-index 1–6, with c-index 1 and 6 denoting apical iodides and c-index 2–5 corresponding to the equatorial plane). In the pristine perovskite lattice, these angles adopt well-defined orientations associated with the high-symmetry octahedral framework. Deviations and broadening of the ϕ distributions indicate in-plane rotations and torsional distortions of the PbI_6 octahedra caused by radiation-induced iodine displacements. These ϕ distributions thus provide a quantitative measure of octahedral *rotational modes*, complementing the θ angle analysis of out-of-plane tilts, and together reveal the extent of tilt and rotational disorder introduced during radiation damage events.

indicating that the lattice preserves its chemical order even under extreme localized heating. This preference for vacancy-interstitial repair over cation/anion mixing is a critical feature of the material’s radiation tolerance.This indicates that the ’soft’ perovskite lattice accommodates highly energetic collision cascades primarily through the high mobility and subsequent re-incorporation of halide ions, effectively healing a significant fraction of the vacancy-interstitial pairs generated during the initial impact.

We observed that the perovskite lattice was able to respond to (and mitigate) the impact of the energy into the lattice by tilting and rotating the halide atoms in the PbI_6 octahedra, a phenomenon that we have not seen discussed previously. We were able to directly connect the macroscopic depth of impact with the extent of tilting and rotating. We were able to assess not only the number of defects created but also the structural pathways through which $CsPbI_3$ perovskites accommodate and largely self-heal radiation-induced damage. Octahedral tilting and rotating (spinning) is thus a very effective way for the “soft” lattice to accommodate the additional energy without permanent amorphization, at least for the energy range studied here (1 eV to 1000 eV).

The role of lattice softness in enabling this radiation tolerance becomes clear when $CsPbI_3$ is contrasted with conventional rigid semiconductors using the extensive MD radiation damage literature. In crystalline Si, the threshold displacement energy E_d, defined as the minimum PKA energy required to produce a stable Frenkel pair, lies in the range of 13–21 eV depending on crystallographic direction.[15] In addition, sub-keV cascades produce rapid amorphization of the cascade core through irreversible covalent bond breaking.[29] Self-healing in Si on the picosecond timescale is negligible, because covalent bond reconstruction carries a high activation barrier that cannot be overcome by thermal fluctuations at 300 K. The behavior of $CsPbI_3$ under identical PKA energy conditions stands in stark contrast on each of these metrics. The effective displacement threshold for iodine is substantially lower, consistent with the high ionic mobility and low halide Frenkel pair formation energies characteristic of soft ionic lattices.[13] Rather than amorphizing, the lattice dissipates cascade energy through collective octahedral tilting and rotation, preserving short-range connectivity across the entire 1–1000 eV energy range studied. And $\approx$32% of displaced halide atoms recover to lattice sites within 10 ps, a recovery fraction that is essentially zero in covalent semiconductors on the same timescale. These contrasting characteristics demonstrate that the radiation tolerance of $CsPbI_3$ is not incidental but is a direct and quantifiable consequence of the soft, ionic character of the perovskite lattice, which provides low-barrier energy dissipation channels unavailable in rigid covalent semiconductors.[9,16]

From a quantitative standpoint, our simulation framework has provided a multi-faceted and granular picture of the radiation damage process in $CsPbI_3$. The analysis progresses

View Article Online
DOI: 10.1039/D6TA01465H

Open Access Article. Published on 15 June 2026. Downloaded on 6/17/2026 5:59:14 AM.
This article is licensed under a Creative Commons Attribution-NonCommercial 3.0 Unported Licence.

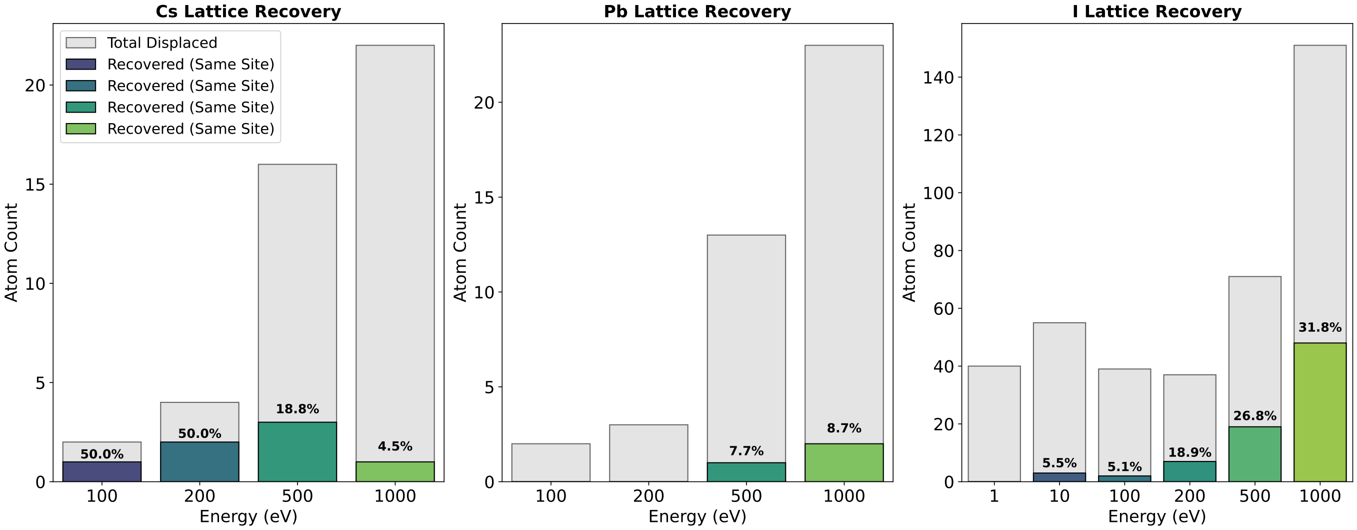

FIG. 11. Lattice recovery statistics as a function of primary knock-on energy for Cs, Pb, and I sublattices. Bars show the total number of atoms displaced by more than 3 Å(gray) as well as the subset that subsequently return to within 2 Åof a lattice site of their original species ("same-site" recovery; colored bars). Percentage values indicate the fraction of displaced atoms that recover to a crystallographically equivalent site of the same atomic type. While Cs and Pb exhibit limited and non-monotonic recovery fractions with increasing energy, I atoms show a pronounced increase in both the absolute number and fraction of recovered atoms at higher energies, reaching ~32% recovery at 1000 eV. Displacement is defined as atomic motion >3 Åfrom the initial position. Recovery is defined as relocation within 2 Åof a lattice site occupied by the same species.

from defect identification to the specific structural distortions that accommodate the impact energy. Steinhardt order parameters are utilized to differentiate the pristine crystalline lattice from disordered regions, allowing for the precise identification and tracking of defect structures generated during the impact cascade. This method quantifies the loss of local bond-orientational order and pinpoints the atoms displaced from their lattice sites.

Our analysis shows that iodine atom displacements are the primary initial manifestation of damage. The sequence and energetic threshold for these displacements are key findings. At low impact energies (*e.g.*, 1-10 eV), the damage is minimal and highly localized, with defects penetrating only ~2 *nm* from the surface and the vast majority of the lattice retaining its crystalline order (as seen in Fig. 6). In stark contrast, high-energy impacts (*e.g.*, 500-1000 eV) initiate a deep damage cascade, creating widespread disorder(as seen in Fig. 5).

The nature of this disorder is quantitatively captured by analyzing the octahedral tilt and rotation.

For octahedra classified as being "changed" as a result of the impact, the distribution of the θ tilt angle shows significant deviations from the pristine state (Fig. 9). While the undistorted lattice exhibits sharp angular peaks, the post-impact distributions broaden considerably, indicating substantial out-of-plane tilting. However, the results cluster around specific, defined angles, suggesting that even within the disordered cascade, the octahedra adopt preferred, metastable tilt configurations rather than a fully amorphous arrangement. This provides a quantitative structural metric for the extent of radiation-induced tilt disorder. Complementing the tilt analysis, the distributions of the in-plane rotational angle, ϕ, also exhibit significant broadening (Fig. 10). This captures the torsional distortions of the PbI_6 octahedra. The cumulative effect of these rotations, or "spin," is visualized in Figure 8, which demonstrates a direct correlation between impact energy and the spatial extent of collective rotational activity. At 1000 eV, intense rotational dynamics penetrate deep into the bulk, mirroring the depth of the defect cascade itself.

These simulation results show a strong correspondence with experimental findings in $CsPbI_3$ nanocrystals[24], where octahedral distortions are similarly identified as a critical factor in determining phase stability and electronic properties[18]. Furthermore, the mechanisms of energy dissipation and the potential for self-healing through localized, recoverable distortions align well with our previous work on low-energy defect pathways in $CsPbBr_3$.[14] Finally, it is important to acknowledge that this highly detailed, atomistic-level quantitative analysis was made possible by the robust capabilities of the ReaxFF reactive force field.[28] Its ability to accurately model the complex bond-breaking and reformation processes during the energetic cascade was crucial for capturing the nuanced structural pathways through which this soft perovskite lattice dissipates energy.

From a practical standpoint, this work offers several concrete guideposts for experimentalists working on perovskite space photovoltaics. The sublattice-resolved recovery fractions reported here as a function of PKA energy provide a quantitative prediction of which irradiation energy regimes and which atomic species are most likely to produce permanent structural degradation, directly informing the design of accelerated aging protocols and the interpretation of post-irradiation structural characterization. The correspondence

Journal of Materials Chemistry A Accepted Manuscript

View Article Online
DOI: 10.1039/D6TA01465H

Open Access Article. Published on 15 June 2026. Downloaded on 6/17/2026 5:59:14 AM.
This article is licensed under a Creative Commons Attribution-NonCommercial 3.0 Unported Licence.

between radiation-induced angular distortions and classical Glazer tilt systems provides a framework for interpreting diffuse X-ray scattering and pair distribution function (PDF) measurements on irradiated perovskite films, since the tilt signatures identified here are, in principle, detectable by these techniques. Finally, the dominance of halide Frenkel pairs over cation anti-sites and amorphous regions as the primary radiation damage product suggests that experimental probes sensitive to halide vacancy populations, such as thermally stimulated current measurements, time-resolved photoluminescence, and impedance spectroscopy, are the most informative tools for tracking radiation damage accumulation and recovery in this class of material.[13,47] Extension of this computational framework to other perovskite compositions, including mixed-cation and 2D perovskite systems, will require the development of validated reactive or machine-learned interatomic potentials for those compositions, which we identify as a key priority for future work in this area.[23]

V. ACKNOWLEDGEMENTS

Research was sponsored by the Army Research Laboratory and was accomplished under Cooperative Agreement Number W911NF-23-2-0062. The views and conclusions contained in this document are those of the authors and should not be interpreted as representing the official policies, either expressed or implied, of the Army Research Laboratory or the U.S. Government. The U.S. Government is authorized to reproduce and distribute reprints for Government purposes notwithstanding any copyright notation herein.

This work was supported by the U.S. Department of Energy, Office of Science, Basic Energy Sciences program. Computational resources and data management support were provided by the Institute for Data Intensive Engineering and Science (IDIES) at Johns Hopkins University through the SciServer platform. This work was also partially supported by a seed grant from the Hopkins Extreme Material Institute and Johns Hopkins Applied Physics Laboratory. The authors are grateful for insightful discussions with colleagues that helped refine the analysis and interpretation of the results.

Journal of Materials Chemistry A Accepted Manuscript

View Article Online
DOI: 10.1039/D6TA01465H

Open Access Article. Published on 15 June 2026. Downloaded on 6/17/2026 5:59:14 AM.
This article is licensed under a Creative Commons Attribution-NonCommercial 3.0 Unported Licence.

REFERENCES

[1] K. Sekar, R. Manisekaran, O. M. Nwakanma, and M. Babudurai, “Significance of formamidinium incorporation in perovskite composition and its impact on solar cell efficiency: A mini-review,” Advanced Energy and Sustainability Research **5**, 2400003 (2024), https://advanced.onlinelibrary.wiley.com/doi/pdf/10.1002/aesr.202400003.

[2] M. T. Hoang, Y. Yang, B. Tuten, and H. Wang, “Are metal halide perovskite solar cells ready for space applications?” The Journal of Physical Chemistry Letters (2022).

[3] Y. Tu, J. Wu, G. Xu, X. Yang, R. Cai, Q. Gong, R. Zhu, and W. Huang, “Perovskite solar cells for space applications: Progress and challenges,” Advanced Materials **33** (2021), 10.1002/adma.202006545.

[4] M. A. Green, A. Ho-Baillie, and H. J. Snaith, “The emergence of perovskite solar cells,” Nature Photonics **8**, 506–514 (2014).

[5] A. Kojima, K. Teshima, Y. Shirai, and T. Miyasaka, “Organometal halide perovskites as visible-light sensitizers for photovoltaic cells,” Journal of the American Chemical Society **131**, 6050–6051 (2009).

[6] A. Ho-Baillie, H. Sullivan, T. Bannerman, H. Talathi, J. Bing, S. Tang, A. Xu, D. Bhattacharyya, I. Cairns, and D. McKenzie, “Deployment opportunities for space photovoltaics and the prospects for perovskite solar cells,” Advanced Materials Technologies **7** (2021), 10.1002/admt.202101059.

[7] F. Lang, M. Jošt, K. Frohna, E. Köhnen, A. Al-Ashouri, A. Bowman, T. Bertram, A. Morales-Vilches, D. Koushik, E. Tennyson, K. Galkowski, G. Landi, M. Creatore, B. Stannowski, C. Kaufmann, J. Bundesmann, J. Rappich, B. Rech, and S. Stranks, “Proton radiation hardness of perovskite tandem photovoltaics,” Joule **4**, 1054–1069 (2020).

[8] W. Delmas, S. Erickson, J. Arteaga, M. Woodall, M. Scheibner, S. Ghosh, and T. Krause, “Evaluation of hybrid perovskite prototypes after 10-month space flight on the international space station,” Advanced Energy Materials **13** (2023), 10.1002/aenm.202203920.

[9] M. Holland, A. Ruth, K. Mielczarek, V. V. Dhas, J. J. Berry, and M. D. Irwin, “Metal halide perovskites demonstrate radiation hardness and defect healing in vacuum,” ACS Applied Materials & Interfaces (2022), 10.1021/acsami.1c24709.

[10] I. Cardinaletti, T. Vangerven, S. Nagels, R. Cornelissen, D. Schreurs, J. Hruby, J. Vodnik, D. Devisscher, J. Kesters, J. D’Haena, A. Franquet, V. Spampinato, T. Conard, W. Maes, W. Deferme, and J. V. Manca, “Organic and perovskite solar cells for space applications,” Solar Energy Materials and Solar Cells **182**, 121–127 (2018).

[11] A. R. Kirmani, D. P. Ostrowski, K. T. VanSant, T. A. Byers, R. C. Bramante, K. N. Heinselman, J. Tong, B. Stevens, W. Nemeth, K. Zhu, I. R. Sellers, B. Rout, and J. M. Luther, “Metal oxide barrier layers for terrestrial and space perovskite photovoltaics,” Nature Energy **8**, 191–202 (2023).

[12] D.-T. Nguyen, D. Walter, K. Weber, T. Duong, and T. White, “Simulating proton radiation tolerance of perovskite solar cells for space applications,” Advanced Energy and Sustainability Research (2023), 10.1002/aesr.202300085.

[13] J. Kang and L. W. Wang, “High Defect Tolerance in Lead Halide Perovskite CsPbBr3,” Journal of Physical Chemistry Letters **8**, 489–493 (2017), publisher: American Chemical Society.

[14] K. Miskin, Y. Cao, M. Marland, F. Shaikh, D. T. Moore, J. A. Marohn, and P. Clancy, “Low-energy pathways lead to self-healing defects in cspbbr3,” Phys. Chem. Chem. Phys. **27**, 15446–15459 (2025).

[15] K. Nordlund, S. J. Zinkle, A. E. Sand, F. Granberg, R. S. Averback, R. E. Stoller, T. Suzudo, L. Malerba, F. Banhart, W. J. Weber, F. Willaime, S. L. Dudarev, and D. Simeone, “Primary radiation damage: A review of current understanding and models,” Journal of Nuclear Materials **512**, 450–479 (2018).

[16] A. R. Kirmani, B. K. Durant, J. Grandidier, N. M. Haegel, M. D. Kelzenberg, Y. M. Lao, M. D. McGehee, L. McMillon-Brown, D. P. Ostrowski, T. J. Peshek, B. Rout, I. R. Sellers, M. Steger, D. Walker, D. M. Wilt, K. T. VanSant, and J. M. Luther, “Countdown to perovskite space launch: Guidelines to performing relevant radiation-hardness experiments,” Joule **6**, 1015–1031 (2022).

[17] J. Wiktor, P. Erhart, E. Fransson, and D. Kubicki, “Quantifying dynamic tilting in halide perovskites: chemical trends and local correlations,” Chemistry of Materials (2023), 10.1021/acs.chemmater.3c00933.

[18] R. A. Saha, M. B. Roeffaers, A. Papadopoulou, B. Goderis, J. Rubio-Zuazo, J. Genoe, and C. Meneghini, “Generating a stable higher-symmetry cspbi3 perovskite phase in ambient conditions: unveiling the role of dimethylammonium iodide and spontaneous strain,” ACS Nano (2025), 10.1021/acsnano.5c07700.

[19] J. S. Bechtel and A. Van der Ven, “Octahedral tilting instabilities in inorganic halide perovskites,” Physical Review Materials **2** (2018), 10.1103/PhysRevMaterials.2.025401.

[20] M. Pols, J. M. Vicent-Luna, I. Filot, A. C. T. van Duin, and S. Tao, “Atomistic insights into the degradation of inorganic halide perovskite cspbi3: A reactive force field molecular dynamics study,” The Journal of Physical Chemistry Letters **12**, 5519–5525 (2021), pMID: 34096726, https://doi.org/10.1021/acs.jpclett.1c01192.

[21] C. Zhang, C. Lu, Z. Jing, C. Wu, J.-P. Piquemal, J. W. Ponder, and P. Ren, “Amoeba polarizable atomic multipole force field for nucleic acids,” Journal of Chemical Theory and Computation **14**, 2084–2108 (2018), pMID: 29438622, https://doi.org/10.1021/acs.jctc.7b01169.

[22] N. N. Intan, B. A. Sorenson, Y. K. Choi, J. J. Choi, J. L. Fulton, N. Govind, S. D. Kelly, G. K. Schenter, P. Clancy, and C. J. Mundy, “Smaller is better: The case for lower-order iodoplumbate species dominating mapbi3/dimethylformamide solutions,” Chemistry of Materials **36**, 8424–8436 (2024), https://doi.org/10.1021/acs.chemmater.4c01523.

[23] M. Pols, A. C. T. van Duin, S. Calero, and S. Tao, “Mixing i and br in inorganic perovskites: Atomistic insights from reactive molecular dynamics simulations,” The Journal of Physical Chemistry C **128**, 4111–4118 (2024), https://doi.org/10.1021/acs.jpcc.4c00563.

[24] A. Matuhina, G. K. Grandhi, M. Liu, J.-H. Smått, N. S. M. Viswanath, H. Ali-Löytty, K. Lahtonen, and P. Vivo, “Octahedral distortion driven by cspbi3 nanocrystal reaction temperature – the effects on phase stability and beyond,” Nanoscale **13**, 14186–14196 (2021).

[25] R. Elmasri and S. B. Navathe, *Fundamentals of database systems* (Pearson, 2015).

[26] G. Ciccotti, C. Dellago, M. Ferrario, E. R. Hernández, and M. E. Tuckerman, “Molecular simulations: past, present, and future (a topical issue in epjb),” The European Physical Journal B **95**, 3 (2022).

[27] A. P. Thompson, H. M. Aktulga, R. Berger, D. S. Bolintineanu, W. M. Brown, P. S. Crozier, P. J. in ’t Veld, A. Kohlmeyer, S. G. Moore, T. D. Nguyen, R. Shan, M. J. Stevens, J. Tranchida, C. Trott, and S. J. Plimpton, “Lammps - a flexible simulation tool for particle-based materials modeling at the atomic, meso, and continuum scales,” Computer Physics Communications **271**, 108171 (2022).

[28] A. C. T. van Duin, S. Dasgupta, F. Lorant, and W. A. Goddard, “Reaxff: a reactive force field for hydrocarbons,” The Journal of Physical Chemistry A **105**, 9396–9409 (2001), https://doi.org/10.1021/jp004368u.

[29] K. Nordlund, S. J. Zinkle, A. E. Sand, F. Granberg, R. S. Averback, R. Stoller, T. Suzudo, L. Malerba, F. Banhart, W. J. Weber, F. Willaime, S. L. Dudarev, and D. Simeone, “Improving atomic displacement and replacement calculations with physically realistic damage models,” Nature Communications **9**, 1084 (2018).

[30] J. Fan, Q. Tan, and J. Hao, “Analysis of displacement damage mechanism and simulation proton irradiation on gaas,” AIP Advances **12**, 095304 (2022), https://pubs.aip.org/aip/adv/article-pdf/doi/10.1063/5.0104457/16476177/095304$_{1o}nline.pdf$.

[31] R. Duke, V. Bhat, and C. Risko, “Data storage architectures to accelerate chemical discovery: data accessibility for individual laboratories and the community,” Chem. Sci. **13**, 13646–13656 (2022).

[32] `https://www.sciserver.org`.

[33] M. Taghizadeh-Popp, J. Kim, G. Lemson, D. Medvedev, M. Raddick, A. Szalay, A. Thakar, J. Booker, C. Chhetri, L. Dobos, and M. Rippin, “Sciserver: A science platform for astronomy and beyond,” Astronomy and Computing **33**, 100412 (2020).

[34] `http://github.com/sciserver/opensciserver`.

[35] P. Jupyter, “Jupyterlab: A next-generation notebook interface,” (2018), version 4.5, Accessed: 2025-12-23.

[36] T. Kluyver, B. Ragan-Kelley, F. Pérez, B. Granger, M. Bussonnier, J. Frederic, K. Kelley, J. Hamrick, J. Grout, S. Corlay, P. Ivanov, D. Avila, S. Abdalla, and C. Willing, “Project jupyter: Jupyter notebook,” `https://jupyter.org` (2016), accessed: 2025-12-23.

[37] `https://parquet.apache.org/docs/`.

[38] These timings are indicative rather than formal benchmarks and were obtained using the same compute environment and data store.

Journal of Materials Chemistry A Accepted Manuscript

View Article Online
DOI: 10.1039/D6TA01465H

Open Access Article. Published on 15 June 2026. Downloaded on 6/17/2026 5:59:14 AM.
This article is licensed under a Creative Commons Attribution-NonCommercial 3.0 Unported Licence.

[39] `https://pandas.pydata.org/docs/user_guide/index.html`.

[40] `https://duckdb.org`.

[41] See `https://www.sciserver.org/datasets/materials/perovskites` for details on how to access the data.

[42] `https://github.com/pclancy-lab/perovskites_space`.

[43] A. M. Glazer, "The classification of tilted octahedra in perovskites," Acta Crystallographica Section B **28**, 3384–3392 (1972), https://onlinelibrary.wiley.com/doi/pdf/10.1107/S0567740872007976.

[44] C. J. Howard and H. T. Stokes, "Group-theoretical analysis of octahedral tilting in perovskites," Acta Crystallographica Section B **54**, 782–789 (1998), https://onlinelibrary.wiley.com/doi/pdf/10.1107/S0108768198004200.

[45] X. Liang, J. Klarbring, W. J. Baldwin, Z. Li, G. Csányi, and A. Walsh, "Structural dynamics descriptors for metal halide perovskites," The Journal of Physical Chemistry C **127**, 19141–19151 (2023), https://doi.org/10.1021/acs.jpcc.3c03377.

[46] P. J. Steinhardt, D. R. Nelson, and M. Ronchetti, "Bond-orientational order in liquids and glasses," Phys. Rev. B **28**, 784–805 (1983).

[47] B. K. Durant, H. Afshari, S. Singh, and I. R. Sellers, "Tolerance of perovskite solar cells to targeted proton irradiation and electronic ionization-induced degradation," ACS Energy Letters (2021), 10.1021/acsenergylett.1c00756.

[48] C. Wang, D. Qu, B. Zhou, C. Shang, X. Zhang, Y. Tu, and W. Huang, "Self-healing behavior of the metal halide perovskites and photovoltaics," Small **20**, 2307645 (2024), https://onlinelibrary.wiley.com/doi/pdf/10.1002/smll.202307645.

Journal of Materials Chemistry A Accepted Manuscript

View Article Online
DOI: 10.1039/D6TA01465H

Open Access Article. Published on 15 June 2026. Downloaded on 6/17/2026 5:59:14 AM.
This article is licensed under a Creative Commons Attribution-NonCommercial 3.0 Unported Licence.

All molecular dynamics trajectories, processed datasets, and analysis scripts supporting the findings of this study are publicly available.

The complete post-processing and analysis framework, including SQL ingestion scripts, DuckDB query workflows, figure-generation notebooks, and full database schema definitions, is available in a public GitHub repository at:

https://github.com/pclancy-lab/perovskites_space

The raw LAMMPS dump files (ASCII format) and compressed Apache Parquet files used for SQL-based analysis are publicly hosted via the SciServer platform and can be accessed at:

https://www.sciserver.org/datasets/materials/perovskites/

The dataset includes:

- Full trajectory data for all primary knock-on atom (PKA) energies investigated (1–1000 eV)
- Converted columnar Parquet files used for database ingestion
- Derived relational tables containing octahedral indices, displacement statistics, and defect metrics

All data are provided in formats compatible with the open-source workflow described in the manuscript, enabling full reproducibility of defect counting, octahedral tilt (θ) and rotation (φ) analyses, spatial defect mapping and recovery stats.

The workflow is system-agnostic and can be directly adapted to other LAMMPS-generated trajectories.

Journal of Materials Chemistry A Accepted Manuscript